

Viscoplastic fingers and fractures in a Hele-Shaw cell

T.V. Ball^{a,*}, N.J. Balmforth^a, A. Dufresne^a

^a *Department of Mathematics, University of British Columbia, Vancouver, BC, V6T 1Z2, Canada*

Abstract

A summary is provided of the theoretical description of two instabilities that may arise in radial displacement flows of yield-stress fluid in a Hele-Shaw cell: the viscoplastic Saffman-Taylor instability and a recently proposed extensional flow instability of shear-thinning fluids. The latter has been identified previously in the context of the two-dimensional flow of a cylinder of power-law fluid; here we extend the analysis to the Herschel-Bulkley model, conjecturing that it may be relevant in Hele-Shaw cells when there is a substantial amount of effective slip. With this background in mind, a variety of experiments are performed in which an aqueous suspension of Carbopol is displaced, or displaces, a Newtonian fluid. The Saffman-Taylor instability is observed, but not the extensional flow instability. When the Carbopol is in contact with water, rather than either air or another immiscible liquid, other instabilities appear that take the form of localized tears or fractures of the Carbopol when that material is placed under tension. The fractures lead to a rich range of patterns within the cell that we attribute to a reduction in the fracture energy of the suspension when in contact with another water-based fluid.

1. Introduction

The so-called Saffman-Taylor instability [1] is well-known to lead to labyrinthian fingering patterns when a viscous fluid emplaced in a narrow conduit is displaced by a second, less viscous fluid. The simplest visualization of this phenomenon is provided by emplacing the more viscous fluid in a thin rectangular slot, or Hele-Shaw cell, and then (radially) pumping in the second fluid [2, 3, 4], or simply pulling apart the walls allowing air to displace the fluid interface (a popular device that has found its way into art installations). This type of fingering instability has also been studied for complex fluids, including both viscoelastic liquids [5, 6] and yield-stress fluids [7, 8, 9, 10, 11, 12, 13, 28, 27], with potential applications to oil extraction from porous media in the petroleum industry.

Fingering patterns with a different origin have also recently been suggested to arise when the displacing fluid is the more viscous, but *shear thinning* [14, 15]: Sayag & Worster performed a theoretical analysis using a power-law fluid to complement an experiment in which Xanthan gum spread out on top of a bath of salty water. Although the gum therefore expanded as a shallow current, they ignored the resulting thickness variations and drew an analogy between the expanding edge and the surface of a cylinder pumped out from an axisymmetrical source. A linear stability analysis of that two-dimensional configuration revealed an instability of shear-thinning power-law fluids.

Sayag & Worster thereby rationalized a dramatic fingering phenomenon that they observed in the experiments.

It should be stressed that the instability explored by Sayag & Worster is two-dimensional and should not operate in a Hele-Shaw cell: for such narrow conduits, when the displacing fluid is viscoplastic and of higher effective viscosity (the opposite of the Saffman-Taylor configuration), Coussot [7] demonstrated that the interface is linearly stable. The difference, of course, lies in the transverse structure of the flow in the Hele-Shaw cell: fluid driven down a narrow conduit must flow over the walls, and with a no-slip condition the shear rate and stresses across the cell play the dominant role in the rheology and dynamics. By contrast, for the two-dimensional expanding cylinder, the extensional flow and stresses are key.

Nevertheless, complex fluids often suffer from the phenomenon of effective slip: the migration of constituent particles away from bounding walls leaves relatively dilute layers that can effectively lubricate the bulk of the fluid [16]. In some situations, the slip is so extreme to prompt the emergence of novel fluid mechanical effects. One therefore wonders whether sufficient wall slip may weaken the dominance of shear rates and stresses in a Hele-Shaw cell and permit the emergence of Sayag & Worster's instability in radial displacement flows. Indeed, it has been suggested previously that sliding prompted by effective slip in conjunction with this instability may be responsible for the development of weakly non-axisymmetrical patterns in gravity currents of Carbopol [17].

In the current paper, we therefore undertake an experimental exploration of the fingering patterns created by viscoplastic radial displacement flows in a Hele-Shaw cell. We consider both the Saffman-Taylor configuration, to ex-

*Corresponding author: *E-mail:* tvball@math.ubc.ca, *Telephone:* 604 827 3034

amine the viscoplastic version of classical fingering, and the inverse, to gauge whether shear-thinning extensional flow instability may arise because of slip. We open our discussion with theoretical background, generalizing the Sayag & Worster analysis to a Herschel-Bulkley fluid, and providing details of the viscoplastic Saffman-Taylor problem that advance beyond previous work.

In our experiments, the working fluids are mainly aqueous suspensions of Carbopol in combination with either air or water. We expose a variety of patterns that form in the displacement flows, many of which are **not** driven by instabilities of either the Saffman-Taylor or shear-thinning extensional flow variety. Instead, we argue that the Carbopol gel actually fractures in a solid-like manner when in contact with water and under tension. This leads to a rich range of fracturing patterns. Only when we use either air or an immiscible liquid does the Carbopol resist fracture and the conventional Saffman-Taylor instability appear. In none of the experiments is there any suggestion that a shear-thinning extensional flow instability is present.

Visco-elastic fracture has previously been suggested to arise in displacement flows of other complex fluids in Hele-Shaw cells [18, 19, 20, 9, 21]. However, this was claimed to develop as a natural variation on the Saffman-Taylor theme, with no critical dependence on whether the second fluid is water-based (although van Damme *et al.* point out the significance of whether the materials are miscible or not). By contrast, for our Carbopol suspensions, we show that the fracturing is definitely distinct from Saffman-Taylor-type fingering and is critically sensitive to the presence of water at the interface, along similar lines to a number of other problems [22, 23, 24].

2. Theoretical pre-amble

For viscoplastic flow down a narrow slot, two limits are possible for the flow structure depending on the degree of slip over the walls: if there is no slip, the configuration corresponds to the viscoplastic version of the classical Hele-Shaw cell; when free sliding is permitted over the walls, the problem becomes equivalent to two-dimensional viscoplastic flow. In either case, we may consider an idealized problem in which an initially axisymmetrical volume of viscoplastic fluid is pumped radially outward or inwards within the cell. The viscoplastic fluid is buffered at either its outer or inner edge, or both, by a Newtonian fluid of relatively small viscosity. In the celebrated Saffman-Taylor configuration, the yield-stress material is displaced by the Newtonian fluid; in Sayag & Worster's extensional flow configuration, the viscoplastic fluid displaces the viscous fluid. We deal with the latter case first.

2.1. Two-dimensional shear-thinning, extensional flow

We consider a Herschel-Bulkley fluid that is pumped into the cell with flux \mathcal{Q} through a central hole of radius r_v . The cell has thickness \mathcal{H} . The constitutive law contains the

consistency factor K , power-law index n and yield stress τ_Y . We write the governing equations in dimensionless form, using the characteristic scale $\mathcal{L} = r_v$ to scale lengths, a velocity scale $\mathcal{V} = \mathcal{Q}/(2\pi\mathcal{L}\mathcal{H})$, timescale \mathcal{L}/\mathcal{V} and stress scale $K(\mathcal{V}/\mathcal{L})^n$. In the inertialess limit, force balance and incompressibility then demand

$$p_r = \frac{1}{r^2} \frac{\partial}{\partial r} (r^2 \tau_{rr}) + \frac{1}{r} \frac{\partial \tau_{r\theta}}{\partial \vartheta}, \quad (1)$$

$$p_\vartheta = \frac{1}{r} \frac{\partial}{\partial r} (r^2 \tau_{r\theta}) + \frac{\partial \tau_{\theta\theta}}{\partial \vartheta} \quad (2)$$

and

$$(ru)_r + v_\vartheta = 0, \quad (3)$$

where p and $\{\tau_{rr}, \tau_{r\theta}, \tau_{\theta\theta}\}$ denote the pressure and deviatoric stress components, and (u, v) is the velocity field. Assuming that the fluid always remains yielded as it is driven through the cell (demanding $\tau_{rr}^2 + \tau_{r\theta}^2 > \text{Bi}^2$), the constitutive law can be written as

$$[\tau_{rr}, \tau_{r\theta}] = \left(\dot{\gamma}^{n-1} + \frac{\text{Bi}}{\dot{\gamma}} \right) [2u_r, (u_\vartheta - v)/r + v_r], \quad (4)$$

where

$$\dot{\gamma} = \sqrt{4u_r^2 + [(u_\vartheta - v)/r + v_r]^2} \quad (5)$$

and the Bingham number is

$$\text{Bi} = \frac{\tau_Y \mathcal{L}^n}{K \mathcal{V}^n}. \quad (6)$$

The outer radius of the fluid is given by $r = R(\vartheta, t)$. Here, the kinematic and stress conditions demand

$$R_t + \frac{v}{R} R_\vartheta = u, \quad (7)$$

$$\left(1 + \frac{R_\vartheta^2}{R^2} \right) p - \left(1 - \frac{R_\vartheta^2}{R^2} \right) \tau_{rr} + 2 \frac{R_\vartheta}{R} \tau_{r\theta} = 0 \quad (8)$$

and

$$\left(1 - \frac{R_\vartheta^2}{R^2} \right) \tau_{r\theta} + 2 \frac{R_\vartheta}{R} \tau_{rr} = 0, \quad (9)$$

in the absence of any interfacial tension or forces exerted by the adjacent fluid.

2.1.1. Stability theory

When the flow remains axisymmetrical, a base outflow is established with

$$u = \frac{1}{r}, \quad R = \sqrt{1 + 2t}, \quad \dot{\gamma} = \frac{2}{r^2}, \quad \tau_{rr} = -\text{Bi} - \frac{2^n}{r^{2n}}, \quad (10)$$

$$p = 2\text{Bi} \ln \left(\frac{R}{r} \right) - \text{Bi} + \frac{2^n}{n} (1 - n) r^{-2n} - \frac{2^n}{n} R^{-2n}. \quad (11)$$

Along the lines summarized by Sayag & Worster, we may analyze the linear stability of this state towards non-axisymmetrical disturbances with azimuthal wavenumber m . The perturbations to the solution in (10)–(11), which

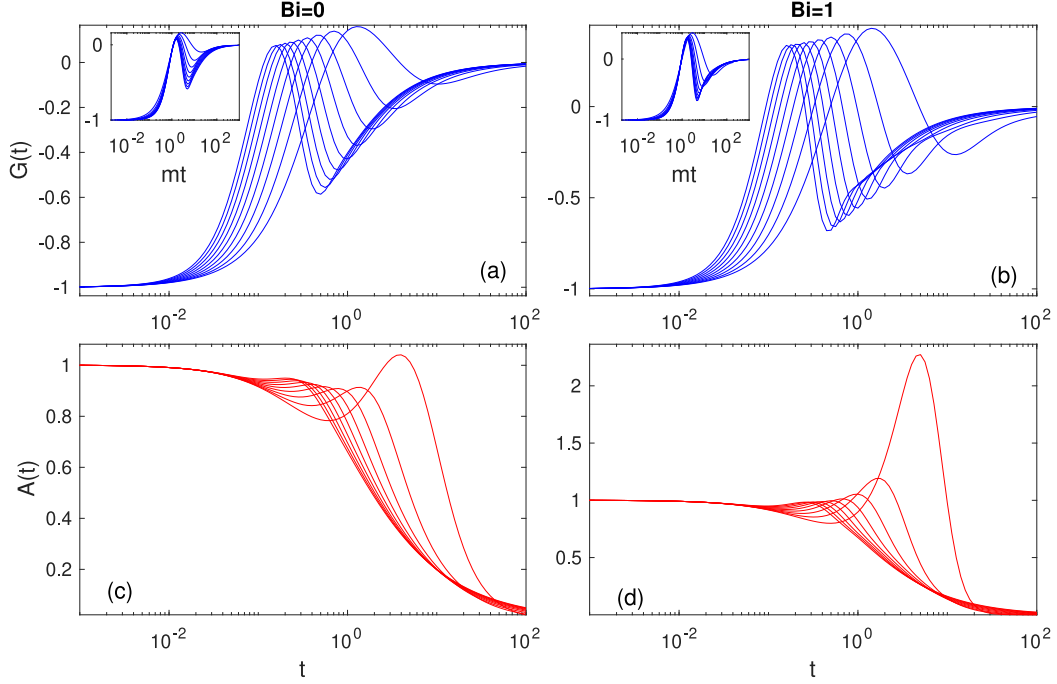


Figure 1: Instantaneous (a,b) growth rates $G(t)$ and (c,d) amplification factors $A(t)$ for $m = 2, 3, 4, \dots, 10$ and $\text{Bi} = 0$ (a,c) and $\text{Bi} = 1$ (b,d); $n = 0.4$. The insets in (a,b) replot the data for $G(t)$ against mt , which aligns the windows of instability (Sayag & Worster).

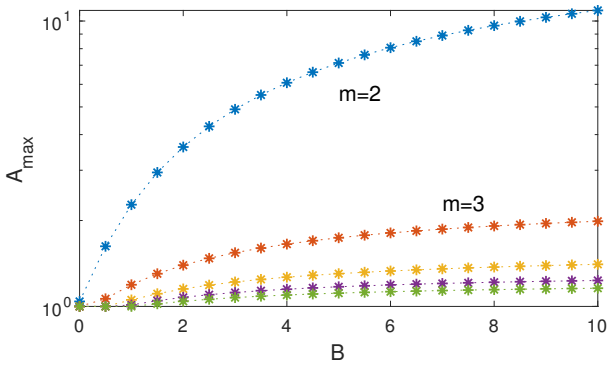


Figure 2: Maximum amplification factors A_{max} over $0 < t < 100$ against Bi for $m = 2, 3, \dots, 6$. ($n = 0.4$)

we denote by adding a hat decoration and with dependence $e^{im\vartheta}$, satisfy the relations,

$$\begin{aligned}
 \frac{\partial}{\partial r}(\hat{\tau}_{rr} - \hat{p}) + \frac{2}{r}\hat{\tau}_{rr} + \frac{1}{r}\frac{\partial\hat{\tau}_{r\vartheta}}{\partial\vartheta} &= 0, \\
 \frac{\partial}{\partial r}\left(r^2\frac{\partial\hat{\tau}_{r\vartheta}}{\partial\vartheta}\right) + m^2r(\hat{\tau}_{rr} + \hat{p}) &= 0, \\
 \hat{u}_r + \frac{1}{r}\hat{u} + \frac{\hat{v}_\vartheta}{r} &= 0, \\
 \left(\frac{\hat{v}_\vartheta}{r}\right)_r - \frac{1}{r\mu}\frac{\partial\hat{\tau}_{r\vartheta}}{\partial\vartheta} - \frac{m^2}{r^2}\hat{u} &= 0,
 \end{aligned} \tag{12}$$

with

$$\mu = 2^{n-1}r^{2-2n} + \frac{1}{2}r^2\text{Bi}, \quad \hat{\tau}_{rr} = -2^n nr^{1-2n} \left(\hat{u} + r \frac{\hat{v}_\vartheta}{r} \right). \tag{13}$$

The boundary conditions are $\hat{u}(1, \vartheta, t) = \hat{v}_\vartheta(1, \vartheta, t) = 0$ (fixed inflow at the vent), and

$$\hat{\tau}_{rr} - \hat{p} + \frac{2}{r}\hat{R} \left(\frac{2^n}{r^{2n}} + \text{Bi} \right) = 0 \tag{14}$$

and

$$r \frac{\partial\hat{\tau}_{r\vartheta}}{\partial\vartheta} + 2m^2\hat{R} \left(\frac{2^n}{r^{2n}} + \text{Bi} \right) = 0 \tag{15}$$

at $r = \sqrt{1 + 2t}$ (the unperturbed outer radius).

As in conventional Stokes problems, the system dynamics enters only through the motion of the boundary; *i.e.* the interface $r = R(\vartheta, t) \rightarrow \sqrt{1 + 2t} + \hat{R}(t)e^{im\vartheta}$. The equations for the linear perturbations can therefore be solved as a spatial problem at each moment in time, with the solution being proportional to $\hat{R}(t)$. The result can then be fed into the kinematic condition, $\hat{R}_t = \hat{u}$, to define an instantaneous growth rate $G(t) = \hat{R}_t/\hat{R}$. Evidently,

$$\hat{R}(t) = \hat{R}(0) \exp \left[\int_0^t G(\hat{t}) d\hat{t} \right] \equiv A(t)\hat{R}(0), \tag{16}$$

where the amplification factor $A(t)$ can be evaluated at some nominal time to furnish a convenient measure of the strength of instability.

Figure 1 displays numerical solutions to the linear stability problem for $m = 2, 3, \dots, 10$, using the rheological parameter settings $n = 0.4$ and $\text{Bi} = 0$ or 1 (such values are guided by the experiments conducted in §3, which use a Carbopol solution with that shear-thinning exponent and operating conditions corresponding to $\text{Bi} = O(1)$). As found by Sayag & Worster, each azimuthal wavenumber

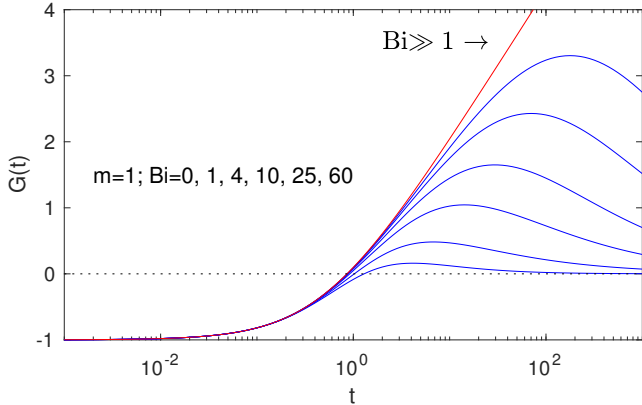


Figure 3: Instantaneous growth rates for the $m = 1$ mode with the values of Bi indicated, as well as the $\text{Bi} \gg 1$ limit. ($n = 0.4$)

passes through an interval over which the instantaneous growth rate is positive, implying mode growth. However, as indicated by the growth factor $A(t)$, for $\text{Bi} = 0$ the actual degree of amplification is small, with only the $m = 2$ mode amplifying above the initial value over its window of instability, and damping over longer times suppressing every mode. Modes grow slightly more significantly with $\text{Bi} = 1$, although the overall picture is much the same. This is emphasized further in figure 2, which shows the maximum possible amplification factor for a selection of modes as a function of Bi . Note that, as observed by Sayag & Worster, the instantaneous growth rate $G(t)$ collapses to a common form for the higher-order modes ($m \gg 1$) when plotted against mt , implying significant limitations on the corresponding amplification factor $A(t)$.

At least with these choices for the rheological parameters, the extensional flow instability therefore seems rather weak, particularly in the limit of a power-law fluid ($\text{Bi} = 0$). The inclusion of surface tension likely suppresses the instability yet further, especially at high wavenumber. The $m = 1$ mode is, however, different: this mode remains unstable over a relatively long interval (see figure 3), sufficient to permit a substantial amount of amplification. Nevertheless, as this mode corresponds mostly to a sideways shift of the expanding fluid column, the instability is not expected to generate a pattern with the form of multiple ‘‘fingers’’.

For large yield stress ($\text{Bi} \gg 1$), we may solve the linear stability problem analytically: from (13) we observe that $\hat{\tau}_{rr}$ remains $O(1)$, whilst \hat{p} and $\hat{\tau}_{r\theta}$ must both become $O(\text{Bi})$ in order to balance the largest terms in (12) and (15). Thus, the first two relations in (12) decouple from the others and imply that

$$\hat{p} \sim \frac{2}{r} \text{Bi} (\cos \Theta + \Gamma \sin \Theta) \quad \& \quad \frac{\partial \hat{\tau}_{r\theta}}{\partial \vartheta} \sim -\frac{2}{r} m^2 \text{Bi} \cos \Theta, \quad (17)$$

in view of the leading-order boundary conditions, where

$$\Theta = \Gamma \log \frac{\sqrt{1+2t}}{r}, \quad \Gamma = \sqrt{m^2 - 1}. \quad (18)$$

These relations can be substituted back into the remain-

der of (12) and (13) to find \hat{u} . After a little algebra, the kinematic condition then furnishes the handy result,

$$\hat{R}^{-1} \frac{d\hat{R}}{dt} = G(t) \sim \frac{1}{\Gamma} \sin[\Gamma \log(1+2t)] - \cos[\Gamma \log(1+2t)]. \quad (19)$$

For $m \gg 1$ and $t \ll 1$, we find $G \rightarrow -\cos(2mt)$, which is analogous to a result provided by Sayag & Worster in the limit $n \ll 1$ for a power-law fluid. However, the result in (19) applies for all wavenumbers and times. The progress of numerically computed growth rates to the $\text{Bi} \gg 1$ limit is illustrated in figure 4 for modes with $m = 4$. The limit in (19) has a curious oscillatory structure, explored in detail by Sayag & Worster. The repeated intervals with positive growth rate highlight how the instability is potentially more powerful in the perfectly plastic limit. Nevertheless, the $m = 1$ mode still dominates over longer times, with the growth rate actually growing logarithmically with t : $G(t) \sim \log(1+2t) - 1$ (cf. figure 3).

2.2. Viscoplastic Hele-Shaw flow

2.2.1. Reduced model

Following classical theory for a Hele-Shaw cell [25], the slot-averaged flux \mathbf{q} satisfies

$$\nabla \cdot \mathbf{q} = 0, \quad \mathbf{q} = -\frac{Q(S; \text{Bi}, n)}{S} \nabla p, \quad (20)$$

where $S = |\nabla p|$, the in-plane gradient operator is ∇ , and the flux function,

$$Q = \frac{1}{n+1} (1-Y)_+^{1+1/n} (n+1+nY) S^{1/n}, \quad (21)$$

with

$$Y = \frac{\text{Bi}}{S}, \quad (1-Y)_+ \equiv \text{Max}(1-Y, 0). \quad (22)$$

The scaling leading to this dimensionless model is provided by scaling pressure p by $12\mu_* \mathcal{V} \mathcal{L} / \mathcal{H}^2$, and the deviatoric stress components by $6\mu_* \mathcal{V} / \mathcal{H}$, where $\mu_* = \frac{1}{3} K (2 + \frac{1}{n})^n (2\mathcal{V} / \mathcal{H})^{n-1}$. The dimensionless yield stress, or Bingham number, is

$$\text{Bi} = \frac{\tau_Y \mathcal{H}}{6\mu_* \mathcal{V}}. \quad (23)$$

The key difference with the two-dimensional theory of §2.1 is that the shear stresses across the slot provide the main resistance to the flow driven by the pressure gradient, establishing a characteristic flow profile across the gap. Provided $Y < 1$, that profile consists of fully sheared layers adjacent to the walls of the cell, sandwiching a central plug-like flow over $-Y < z < Y$; if Y reaches unity (the dimensionless wall position), the plug-like layer fills the gap to form a rigid blockage.

The flux-pressure-gradient relation (21) is illustrated in figure 5 and has two key limits: for $\text{Bi} \rightarrow 0$, $Q \rightarrow S^{1/n}$, corresponding to the limit of a power-law fluid; if, additionally, $n = 1$, $Q \rightarrow S$ and (20) reduces to Laplace’s

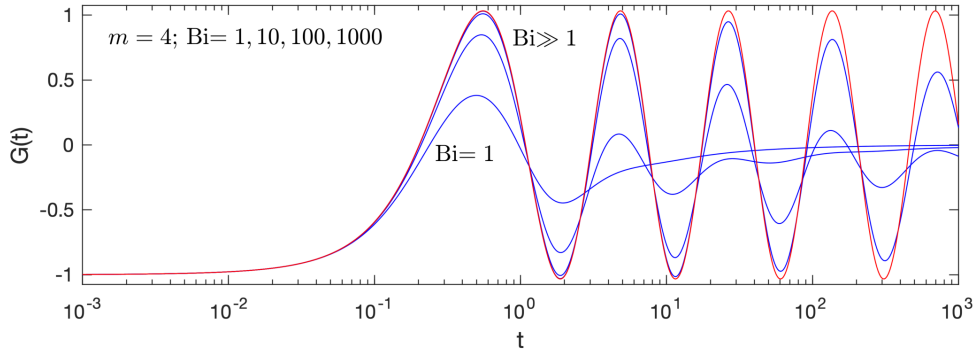


Figure 4: Instantaneous growth rates for the $m = 4$ mode with the values of Bi indicated. The (red) line marked $Bi \gg 1$ shows the prediction (19). ($n = 0.4$)

equation, in the usual manner of viscous Hele-Shaw flow. For $Bi \gg 1$, $Q \rightarrow (2n + 1)(1 - Y)^{1+1/n} Bi^{1/n} / (n + 1)$, which demands that $S = O(Bi)$ and $Y \rightarrow 1$. This limit corresponds to a perfectly plastic material with a specific sliding law applying at the walls dictated by the yielded boundary layers that remain there.

Experimentally, one can conveniently set up a configuration susceptible to Saffman-Taylor fingering by first pumping viscoplastic fluid within the cell, and then switching the feeder tube to pump in a second Newtonian fluid. This creates an expanding annulus of viscoplastic fluid for which the inner edge may lose axisymmetry and develop fingers (*cf.* [26]). To explore this situation theoretically, we therefore consider an annular region contained between inner and outer edges located at $r = R_i(\vartheta, t)$ and $r = R_o(\vartheta, t)$, satisfying the kinematic conditions,

$$\left(\frac{\partial}{\partial t} + \frac{\mathbf{q} \cdot \hat{\boldsymbol{\vartheta}}}{r} \frac{\partial}{\partial \vartheta} \right) R = \mathbf{q} \cdot \hat{\mathbf{r}} \quad \text{at } r = R = R_i \text{ or } R_o. \quad (24)$$

We can also set up another arrangement to study the viscoplastic version of Saffman-Taylor fingering by extracting a disk of yield stress fluid from the cell, with either air or another Newtonian fluid with relatively small viscosity on the outside. For a given flux and at comparable radii, the instantaneous growth rate of disturbances to the unstable interface is not expected to be very different in the two situations. However, in the first case, in which the inner interface is expanding and expected to be unstable, the angular stress of the yield-stress fluid is tensile. Conversely, for the extraction problem, the unstable outer interface has a compressive angular stress. We return later to this important difference.

2.2.2. Stability theory for axisymmetrical flow

When the net dimensionless flux is constant and equal to 2π , an axisymmetrical flow is possible, driven by a local radial pressure gradient, $S \rightarrow \mathcal{S}(r, t)$, satisfying the algebraic relation,

$$\frac{1}{r} = Q(\mathcal{S}; n, Bi). \quad (25)$$

For an expanding annulus, the flux is directed outwards and the pressure gradient is negative. The corresponding circular fluid edges are

$$\begin{aligned} R_i(t) &= \sqrt{1 + 2t} \equiv \mathcal{R}_i(t), \\ R_o(t) &= \sqrt{R_A^2 + 2t} \equiv \mathcal{R}_o(t), \end{aligned} \quad (26)$$

where R_A is the initial outer radius. For an extracted disk, the flux is directed inwards and the background pressure gradient is positive; the single interface is at

$$r = \mathcal{R}(t) = \sqrt{R_A^2 - 2t}, \quad (27)$$

where R_A now denotes its initial position. If we neglect the pressure of the ambient fluid beyond $r = \mathcal{R}_o(\vartheta, t)$ or $r = \mathcal{R}(\vartheta, t)$ then the base pressure distribution is

$$\mathcal{P}(r, t) = \int_r^{\mathcal{R}_o} \mathcal{S}(\tilde{r}) d\tilde{r} \quad \text{or} \quad - \int_r^{\mathcal{R}} \mathcal{S}(\tilde{r}) d\tilde{r}. \quad (28)$$

Linear perturbations to this state, with dependence $e^{im\vartheta}$ and a pressure distinguished by a hat decoration, satisfy

$$(rQ'\hat{p}_r)_r = \frac{m^2\hat{p}}{r\mathcal{S}}Q(\mathcal{S}; n, Bi) \rightarrow \frac{m^2\hat{p}}{r^2\mathcal{S}}, \quad (29)$$

where

$$Q' = \frac{1}{r} \left[\frac{(n+1)}{(n+1)\mathcal{S} + nBi} + \frac{(n+1)}{n(\mathcal{S} - Bi)} - \frac{2}{\mathcal{S}} \right]. \quad (30)$$

2.2.3. An expanding viscoplastic annulus

When a Newtonian fluid with relatively small viscosity is pumped into an annulus of viscoplastic fluid, the pressure within the inner interface is almost uniform in space but adjusts in time so that the net flux through the cell is fixed. To see this in detail, we first solve Laplace's equation for the pressure perturbation in $1 < r < \mathcal{R}_i$, applying a fixed influx condition at the vent $r = 1$ (using the radius of that orifice in the scaling of the problem): $\hat{p}_r(1, t) = 0$. To first order in the perturbations, this gives the pressure

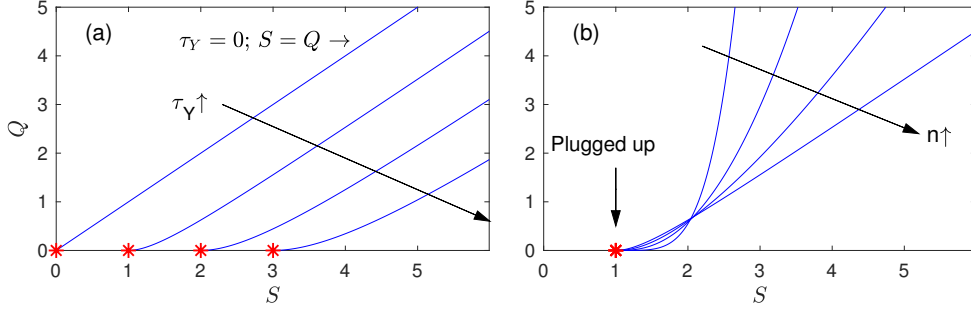


Figure 5: Flux functions for different (a) Bingham numbers $Bi = 0, 1, 2$ and 3 (with $n = 1$) and (b) different power-law exponents $n = \frac{1}{4}, \frac{1}{2},$ and 1 (with $Bi = 1$).

distribution,

$$p(r, t) = \mathcal{P}(\mathcal{R}_I, t) + \frac{\mu}{\mu_*} \log\left(\frac{\mathcal{R}_I}{r}\right) + \frac{r^m + r^{-m}}{\mathcal{R}_I^m + \mathcal{R}_I^{-m}} \hat{p}^{in}(t) e^{im\vartheta}, \quad (31)$$

if μ is the viscosity of the Newtonian fluid, and given that the scaling of the problem implies the local flux-pressure-gradient relation $S = (\mu/\mu_*)Q$. Here, $\hat{p}^{in}(t)$ is the amplitude of the pressure perturbation at $r = \mathcal{R}_I$. Matching pressures and the radial velocity at the inner interface (but expanding all quantities about the unperturbed position) now demands that

$$\hat{p}(\mathcal{R}_I, t) = \left[S(\mathcal{R}_I, t) - \frac{\mu}{\mu_*} \mathcal{R}_I^{-1} \right] \hat{R}_I(t) e^{im\vartheta} + \hat{p}^{in} e^{im\vartheta}. \quad (32)$$

and

$$[Q' \hat{p}_r]_{r=\mathcal{R}_I} = \frac{\mu_*}{\mu} \frac{m(\mathcal{R}_I^{2m} - 1)}{\mathcal{R}_I(\mathcal{R}_I^{2m} + 1)} \hat{p}^{in} e^{im\vartheta}. \quad (33)$$

where $\hat{R}_I e^{im\vartheta}$ denotes the perturbation to the edge position. Eliminating $\hat{p}^{in}(t)$ leads to the boundary condition,

$$\hat{p}(\mathcal{R}_I, t) = \left[S(\mathcal{R}_I, t) - \frac{\mu}{\mu_*} \mathcal{R}_I^{-1} \right] \hat{R}_I(t) e^{im\vartheta} + [Q' \hat{p}_r]_{r=\mathcal{R}_I} \frac{\mu}{\mu_*} \frac{\mathcal{R}_I(\mathcal{R}_I^{2m} + 1)}{m(\mathcal{R}_I^{2m} - 1)}. \quad (34)$$

As long as $m \neq 0$, we may therefore impose $\hat{p} = S \hat{R}_I(t) e^{im\vartheta}$ at $r = \mathcal{R}_I$ when $\mu \ll \mu_*$.

Likewise, at the outer edge, we assume that the pressure is held at that of the ambient fluid (which we again neglect): $p = 0$ at $r = \mathcal{R}_O$. The linearization again implies that $\hat{p} - S \hat{R}_O e^{im\vartheta} = 0$ at $r = \mathcal{R}_O$, where $\hat{R}_O e^{im\vartheta}$ is the shift of the outer edge.

We may therefore find two solutions to (29), $\hat{p}^I(r, t) e^{im\vartheta}$ and $\hat{p}^O(r, t) e^{im\vartheta}$, satisfying the conditions,

$$\hat{p}^I = \begin{cases} S & \text{at } r = \mathcal{R}_I \\ 0 & \text{at } r = \mathcal{R}_O \end{cases}, \quad \hat{p}^O = \begin{cases} 0 & \text{at } r = \mathcal{R}_I \\ S & \text{at } r = \mathcal{R}_O \end{cases}. \quad (35)$$

Writing the edge perturbations as $\hat{R}_I e^{im\vartheta}$ and $\hat{R}_O e^{im\vartheta}$, the desired linear solution is then,

$$\hat{p} = [\hat{R}_I(t) \hat{p}^I(r, t) + \hat{R}_O(t) \hat{p}^O(r, t)] e^{im\vartheta}.$$

The linearizations of the kinematic conditions now furnish the system

$$\frac{d\hat{R}_I}{dt} = - \left[(Q' \hat{p}_r^I + r^{-2}) \hat{R}_I + Q' \hat{p}_r^O \hat{R}_O \right]_{r=\mathcal{R}_I}, \quad (36)$$

$$\frac{d\hat{R}_O}{dt} = - \left[Q' \hat{p}_r^I \hat{R}_I + (Q' \hat{p}_r^O + r^{-2}) \hat{R}_O \right]_{r=\mathcal{R}_O}. \quad (37)$$

2.2.4. Extraction of a viscoplastic disk

For the extraction problem, the theoretical description is simpler: we write $r = R(\vartheta, t) = \mathcal{R}(t) + \hat{R}(t) e^{im\vartheta}$ and $\hat{p} = \hat{p}^A(r, t) \hat{R}(t) e^{im\vartheta}$ for the disturbed interface position and pressure. The linear perturbations satisfy (29) subject to the boundary conditions,

$$\hat{p}_r^A(1) = 0 \quad \& \quad \hat{p}^A(\mathcal{R}, t) = -S(\mathcal{R}), \quad (38)$$

which correspond to specifying the extracted flux at the vent $r = 1$ and fixing the ambient pressure. The linearized kinematic condition then provides the instantaneous growth rate,

$$\hat{R}^{-1} \frac{d\hat{R}}{dt} = -[Q' \hat{p}_r^A]_{r=\mathcal{R}} - \frac{1}{\mathcal{R}^2}. \quad (39)$$

2.2.5. Interfacial tension effects

Interfacial tension (which is often incorporated in order to regularize Saffman-Taylor instability for immiscible fluids) can be included in this analysis simply by replacing S in the two relations in (35) by $S(\mathcal{R}_I) - \kappa_I(m^2 - 1)/\mathcal{R}_I^2$ and $S(\mathcal{R}_O) + \kappa_O(m^2 - 1)/\mathcal{R}_O^2$, where κ_I and κ_O are dimensionless parameters given by the interfacial tensions, γ_I and γ_O :

$$(\kappa_I, \kappa_O) = \frac{\mathcal{H}^2}{12\mu_* \mathcal{V} \mathcal{L}^2} (\gamma_I, \gamma_O). \quad (40)$$

Similarly, in (38), we replace $S(\mathcal{R})$ with $S(\mathcal{R}) - (m^2 - 1)\kappa/\mathcal{R}^2$ for another interfacial tension parameter κ .

2.2.6. Planar instability

We may recover the viscoplastic version of the Saffman-Taylor instability for a single planar interface from (29)

by switching radial derivatives for Cartesian ones on the left-hand side, $r^{-1}(rQ'\hat{p}_r)_r \rightarrow Q'\hat{p}_{xx}$, and introducing the planar transverse wavenumber $\ell \equiv m/r$ on the right. The interface, now at $x = \mathcal{X} + \hat{X}(t)e^{i\ell y}$, travels at a fixed speed Q under a constant pressure gradient of magnitude \mathcal{S} in the absence of the transverse perturbations with amplitude $\hat{X}(t)$. We take the viscoplastic fluid to lie to the left of the interface; when that fluid is advancing, the interface moves to the right with a speed Q and the pressure gradient is $-\mathcal{S}$; in retreat, the interface moves left with speed $-Q$ under a pressure gradient \mathcal{S} . Thence,

$$\hat{p}_{xx} = \frac{\ell^2 Q}{SQ'} \hat{p}, \quad (41)$$

or

$$\hat{p} = -(\sigma\mathcal{S} - \kappa\ell^2)\hat{X} \exp\left(i\ell y + |\ell|\sqrt{\frac{Q}{SQ'}}|x - \mathcal{X}|\right), \quad (42)$$

after linearizing about the undisturbed position of the interface, $x = \mathcal{X}$, given that the pressure condition there becomes $\hat{p} + \sigma\mathcal{S}\hat{X}e^{i\ell y} = \kappa\ell^2\hat{X}e^{i\ell y}$, where κ is again a dimensionless surface tension and $\sigma = \mp 1$ distinguishes the cases of an advancing or retreating interface (*i.e.* indicates the sense of the background pressure gradient). The linearized kinematic condition, $\hat{X}_t = -Q'\hat{p}_x$, now gives

$$\hat{X}_t = |\ell|\sqrt{\frac{QQ'}{\mathcal{S}}}(\sigma\mathcal{S} - \kappa\ell^2)\hat{X}. \quad (43)$$

The retreating interface is therefore unstable to transverse perturbations with wavenumbers $|\ell| < \sqrt{\mathcal{S}/\kappa}$, with the wavelength of maximum growth given by $2\pi/\ell = 2\pi\sqrt{3\kappa/\mathcal{S}}$. Notably, because one must exceed a threshold pressure gradient for force flow, \mathcal{S} remains finite for $Q \rightarrow 0$, and so the most unstable wavelength remains finite in the limit that the flow rate ceases (for finite interfacial tension), in contrast to the viscous version of the problem (*cf.* [7, 8]). In particular, in dimensional terms and the perfectly plastic limit ($\mathcal{S} \rightarrow \text{Bi}$), the most unstable wavelength is $2\pi\mathcal{L}\sqrt{3\kappa/\text{Bi}} = \pi\sqrt{6\mathcal{H}\gamma/\tau_Y}$. Note that the growth rate implied by (43) is a little different from that presented by [7] because we avoid any approximation of the flux-pressure-gradient relation in (21) (similarly the results for radial flow, when restricted to the case of a single interface, are also different from those presented by both [7] and [11]).

2.2.7. Instability in the Newtonian limit

For a Newtonian annulus, the two solutions \hat{p}^I and \hat{p}^O are built from the two independent solutions, $r^{\pm m}$, to

Laplace's equation, leading to

$$\frac{d\hat{R}_I}{dt} = \frac{m(\mathcal{R}_I^{2m} + \mathcal{R}_O^{2m})}{\mathcal{R}_I^2(\mathcal{R}_O^{2m} - \mathcal{R}_I^{2m})\hat{R}_I} - \frac{\hat{R}_I}{\mathcal{R}_I^2} - \frac{2m\mathcal{R}_I^{m-1}\mathcal{R}_O^{m-1}\hat{R}_O}{\mathcal{R}_O^{2m} - \mathcal{R}_I^{2m}}, \quad (44)$$

$$\frac{d\hat{R}_O}{dt} = \frac{\hat{R}_O}{\mathcal{R}_O^2} - \frac{m(\mathcal{R}_O^{2m} + \mathcal{R}_I^{2m})\hat{R}_O}{\mathcal{R}_O^2(\mathcal{R}_O^{2m} - \mathcal{R}_I^{2m})} + \frac{2m\mathcal{R}_I^{m-1}\mathcal{R}_O^{m-1}\hat{R}_I}{\mathcal{R}_O^{2m} - \mathcal{R}_I^{2m}}. \quad (45)$$

When $\mathcal{R}_O \gg \mathcal{R}_I$, the two equations decouple and

$$\frac{d\hat{R}_I}{dt} = \frac{(m-1)\hat{R}_I}{\mathcal{R}_I^2} \quad \& \quad \frac{d\hat{R}_O}{dt} = -\frac{(m+1)\hat{R}_O}{\mathcal{R}_O^2}, \quad (46)$$

which demonstrates the instability of the inner edge (with instantaneous growth rate $(m-1)/\mathcal{R}_I^2$), and the stability of the outer edge. Conversely, for a thin annulus with $\mathcal{R}_O - \mathcal{R}_I \ll 1$, we find

$$\begin{aligned} \frac{d}{dt}(\hat{R}_O + \hat{R}_I) &\sim -\frac{2}{\mathcal{R}_O(\mathcal{R}_O - \mathcal{R}_I)}(\hat{R}_O - \hat{R}_I) \\ \frac{d}{dt}(\hat{R}_O - \hat{R}_I) &\sim -\frac{m^2 - 1}{2\mathcal{R}_O^3}(\mathcal{R}_O - \mathcal{R}_I)(\hat{R}_O + \hat{R}_I), \end{aligned} \quad (47)$$

implying an instantaneous growth rate, $\sqrt{(m^2 - 1)}/\mathcal{R}_O^2$.

In the extraction of a Newtonian disk, on the other hand, the pressure solution is given by $\hat{p} = -(r^m + r^{-m})\hat{R}e^{im\theta}/[\mathcal{R}(\mathcal{R}^m + \mathcal{R}_O^{-m})]$, leading to the instantaneous growth rate,

$$\hat{R}^{-1}\frac{d\hat{R}}{dt} = \frac{(m-1)\mathcal{R}^{2m} - m - 1}{\mathcal{R}^2(\mathcal{R}^{2m} + 1)}. \quad (48)$$

If we set $\mathcal{R} \gg 1$ (corresponding to a relatively small vent) and then include surface tension, we find a growth rate, $(m-1)[1 - m(m+1)\kappa/\mathcal{R}]/\mathcal{R}^2$, which recovers results derived by Wilson [4] (in the limit $\mu \ll \mu_s$) and Paterson [2].

2.2.8. Large yield stress

In the opposite limit of large yield stress,

$$\mathcal{S} \rightarrow \text{Bi} + \left[\frac{(n+1)\text{Bi}}{(2n+1)r}\right]^{n/(n+1)} \quad (49)$$

and

$$Q' \rightarrow \frac{n+1}{nr^{1/(n+1)}} \left[\frac{(2n+1)}{(n+1)\text{Bi}}\right]^{n/(n+1)}, \quad (50)$$

leading to

$$\left[r^{n/(n+1)}\hat{p}_r\right]_r \sim \frac{nm^2\hat{p}}{r^2[(n+1)(2n+1)^n\text{Bi}]^{1/(n+1)}}. \quad (51)$$

Since the right-hand side of (51) is $O(\text{Bi}^{-1/(n+1)})$, we may neglect it to arrive at the two limiting solutions to the annulus problem,

$$(\hat{p}^I, \hat{p}^O) \rightarrow \frac{\text{Bi}(\mathcal{R}_O^{1/(n+1)} - r^{1/(n+1)}, r^{1/(n+1)} - \mathcal{R}_I^{1/(n+1)})}{\mathcal{R}_O^{1/(n+1)} - \mathcal{R}_I^{1/(n+1)}}. \quad (52)$$

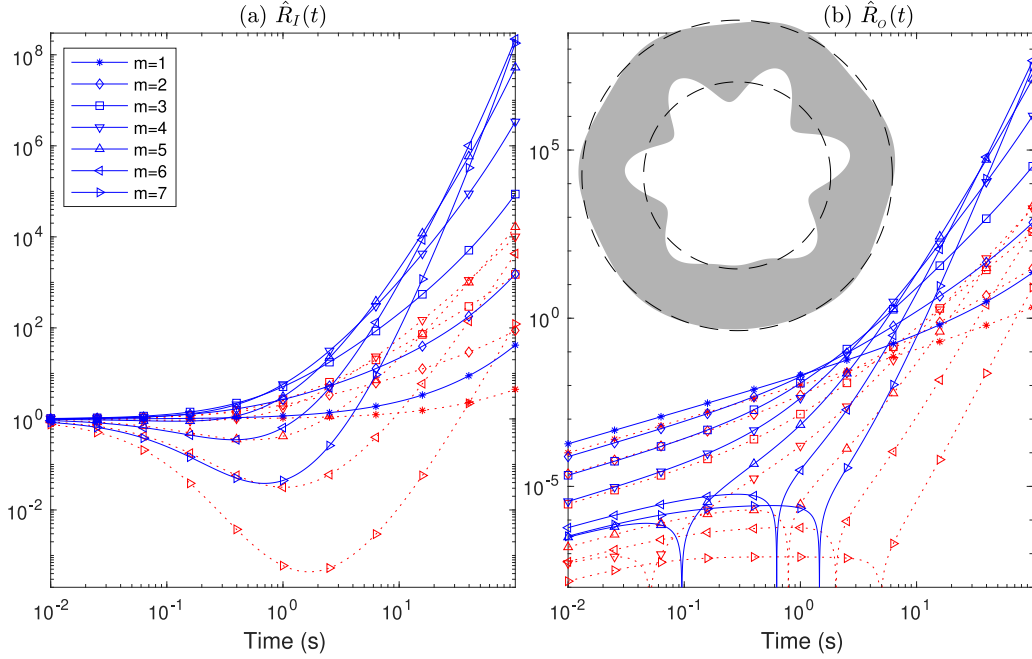


Figure 6: Numerical solutions for an expanding annulus, showing (a) $\hat{R}_I(t)$ and (b) $\hat{R}_O(t)$ for $m = 1, 2, \dots, 7$, starting from the initial conditions $\hat{R}_I(0) = 1$ and $\hat{R}_O(0) = 0$, with $Bi = 0.42$ (blue, solid lines) and $Bi = 0$ (red dotted lines), and $n = 0.4$. Times are shown in seconds, taking $\mathcal{H} = 1.7\text{mm}$, $\mathcal{Q} = 20\text{ml/min}$, and $\mathcal{L} = r_v = 5\text{mm}$ (typical experimental parameters of §3). Interfacial tension is included, assuming $\kappa_I = \kappa_O = 0.07$. The inset in (b) shows a snapshot of the final state, assuming that the different modes in m are linearly superposed and all initialized with amplitudes of $O(10^{-8}\mathcal{L})$ and random phases.

Hence,

$$\begin{aligned} \mathcal{R}_I \frac{d\hat{R}_I}{dt} &\sim \mathcal{R}_O \frac{d\hat{R}_O}{dt} \\ &\sim \frac{(2n+1)^{n/(n+1)} Bi^{1/(n+1)} (\hat{R}_I - \hat{R}_O)}{n(n+1)^{n/(n+1)} [\mathcal{R}_O^{1/(n+1)} - \mathcal{R}_I^{1/(n+1)}]}. \end{aligned} \quad (53)$$

The modulation in the thickness of the annulus therefore amplifies with an instantaneous growth rate,

$$\begin{aligned} (\hat{R}_O - \hat{R}_I)^{-1} \frac{d}{dt} (\hat{R}_O - \hat{R}_I) &\sim \\ &\frac{(2n+1)^{n/(n+1)} Bi^{1/(n+1)} (\mathcal{R}_O - \mathcal{R}_I)}{n(n+1)^{n/(n+1)} \mathcal{R}_I \mathcal{R}_O [\mathcal{R}_O^{1/(n+1)} - \mathcal{R}_I^{1/(n+1)}]}, \end{aligned} \quad (54)$$

which is independent of m . Evidently, the amplification increases with Bi , in line with the notion that the instability grows stronger for a larger effective viscosity contrast across the inner interface. The neglect of the final term in (34) is, however, suspicious in this limit because $Q' \hat{p}_r = O(Bi^{1/(n+1)})$.

For the extracted disk, we must work further with (51), evaluating the right-hand side perturbatively. We find

$$\hat{p} \sim -Bi - \frac{nm^2(nr+1)}{n+1} \left[\frac{(n+1)Bi}{(2n+1)r} \right]^{n/(n+1)}. \quad (55)$$

The instantaneous growth rate is then

$$\hat{R}^{-1} \frac{d\hat{R}}{dt} \sim m^2 \mathcal{R}^{-2} (\mathcal{R} - 1), \quad (56)$$

which is $O(1)$ and dependent on m , but stronger than in the Newtonian limit (comparing (56) with (48)).

2.2.9. Results for $Bi = O(1)$

Numerical solutions of (29) for $\hat{R}_I(t)$ and $\hat{R}_O(t)$ for an expanding annulus with $n = Bi = 0.42$ and $m = 1, 2, \dots, 7$ are shown in figure 6, beginning with the initial conditions, $\hat{R}_I(0) = 1$ and $\hat{R}_O(0) = 0$. The choices for n and Bi are values guided by the experiments in §3.1 (*cf.* figure 8), and interfacial tension is included at both edges, taking $\kappa_I = \kappa_O = 0.07$ (corresponding to adopting the surface tension of water for γ_O and γ_I). The interfacial tension stabilizes the higher modes at early time, but this effect declines as the edges expand and curvatures decreases, until all the modes begin to grow with rates that increase with m . This competition leaves the $m = 6$ mode as the strongest at the end of the computation, as can be seen in the sample pattern formed from the seven modes, obtaining from a linear superposition with equal initial amplitudes of $10^{-8}\mathcal{L}$ and random angular phases. For comparison, solutions with $Bi = 0$ are also shown, which amplify less quickly, in line the expectations from the analysis of the limit of large yield stress.

Solutions for an extracted disk are shown in figure 7 for $(n, Bi) = (0.4, 0.32)$ (parameter settings that are again guided by the experiments of §3.1; figure 8). At smaller times (larger radii), the effect of interfacial tension (parametrized here by setting $\kappa = 0.3$) is relatively low, leaving the higher wavenumber modes as the most un-

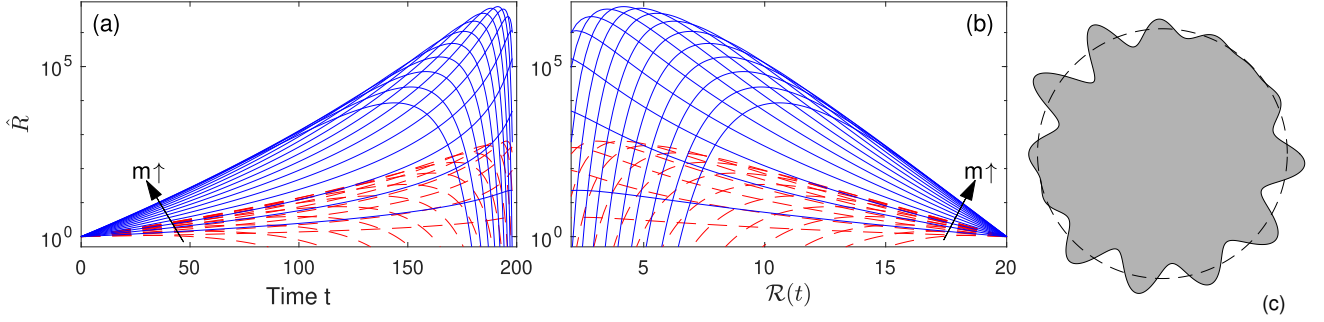


Figure 7: Interface perturbation amplitude $\hat{R}(t)$ for an extracted disk with $R_A = 20$, $m = 1, 2, \dots, 16$, $Bi = 0.32$, $n = 0.4$ and $\kappa = 0.3$. In (a), the amplitudes are plotted against time; $\hat{R}(t)$ is plotted against $\mathcal{R}(t)$ in (b). The dashed (red) lines show the corresponding results for $Bi = 0$. The shape of the interface when the mean radius is about $\frac{1}{2}R_A$ is shown in (c), assuming a linear superposition of the modes with random phases and initial amplitudes of 10^{-5} .

stable. That tension grows in importance due to the increasing curvature of the interface as the disk shrinks, gradually stabilizing the higher- m modes and promoting the importance of the lower angular wavenumbers. The solutions again confirm that the instability is stronger for $Bi > 0$. For the parameters chosen, the most unstable modes have $m = 11$ or 12 when the mean radius of the interface is about half of the initial value.

3. Experiments

Our experiments involved pumping aqueous suspensions of Carbopol (Ultrez 20, with concentrations of between 0.15-0.45% by weight, and neutralized with sodium hydroxide) into or out of a cell made from plexiglass plates. Spacers between the plates furnishes cells with gaps of thickness ranging from 1.7mm to 4.3mm. We used fits to the flow curves obtained from a rheometer (Kinexus Malvern rheometer fitted with roughened parallel plates) to estimate suitable parameters of the Herschel-Bulkley law for the Carbopol solutions.

When the test was aimed at exploring the displacement of a Newtonian fluid by Carbopol, we pumped the gel into either an empty cell (so that the Carbopol displaced air), or first filled the gap with a viscous liquid. When the test demanded that we displace the gel, we began by pumping Carbopol into the cell to form a disk with a given radius. We then either switched the inlet pipe and pumped in a Newtonian fluid to create an expanding viscoplastic annulus, or reversed the pump to extract the Carbopol. In the latter tests, we either left the gap empty to study displacement by air, or surrounded the Carbopol with a displacing viscous liquid.

A first observation is that the Carbopol remains largely axisymmetrical when pumped into an empty (air-filled) cell. Evidently, any imperfections in the surfaces and alignment of the walls are not sufficiently significant to desymmetrize the flow. Moreover, there is no sign that effective slip over the plexiglass plates precipitates the extensional flow instability described by Sayag & Worster.

However, when we displace the gel by air, or place water next to the Carbopol, a variety of different kinds of fingering patterns are observed that are not all related to Saffman-Taylor fingering, as we describe next.

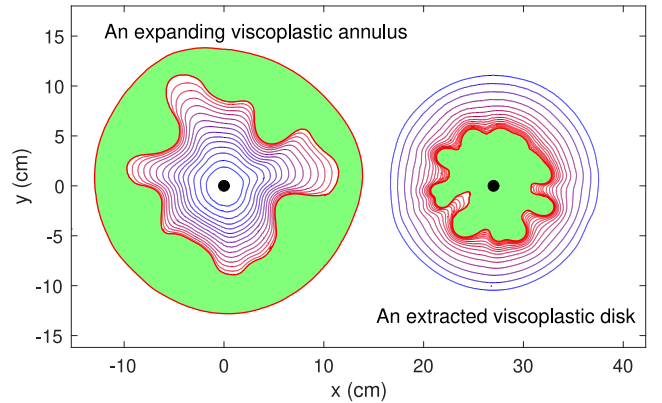


Figure 8: Experiments pumping air into an annulus of Carbopol (left) or withdrawing a disk of Carbopol surrounded by air. Shown are snapshots of the unstable interface, colour coded by time, with the final distribution of Carbopol shown shaded and the vent indicated by a small black disk. (Pump rate $Q \approx 20\text{ml/min}$; gap $H = 1.7\text{mm}$; rheology $(n, \tau_Y, K) = (0.38, 22\text{Pa}, 13\text{Pa s}^n)$.)

3.1. Viscoplastic Saffman-Taylor fingers

The displacement of Carbopol by air provides a convenient illustration of the viscoplastic analogue of classical Saffman-Taylor fingering. Two versions of this problem are shown in figure 8. On the left side of the picture, snapshots of the evolving, unstable interface are displayed that result when air is pumped into an annulus of Carbopol; the interface initially expands axisymmetrically, but then develops a non-axisymmetrical pattern characterized by relatively low angular wavenumbers. At the end of the test, just before the air breaks through the Carbopol into the surrounding empty cell, the pattern has a dominant $m = 8$ component. This relatively weak fingering pattern is suggestive of Saffman-Taylor fingers controlled by

a relatively strong interfacial tension, as expected theoretically in §2.2.9 (see figure 6). Similar results and patterns were found when we pumped immiscible Newtonian fluids into the cell instead of air. In particular, we used mineral spirits and a paraffin-based lamp oil, with viscosities comparable or slightly higher than that of water (about 1 or 2 Pa s, respectively), and tensions at an interface with water expected to be about half the surface tension of water in air.

The second experiment, shown on the right side of figure 8, is a test in which a disk of Carbopol in an air-filled cell is withdrawn through the vent. Again, a finger pattern develops, this time characterized by angular modes with slightly higher wavenumber; just before the strongest finger breaks through to the vent (which occurs when the average radius is about half the initial one), the mode with $m = 12$ or so dominates the pattern. This observation is again consistent with the theoretical expectations of §2.2.9, as shown in figure 7, although these calculations use a value for the surface tension parameter κ that is six times larger than that based on the experimental parameters (assuming the Carbopol has a surface tension comparable to water).

Similar viscoplastic Saffman-Taylor fingering patterns to those in figure 8 are presented by [9] for radial displacement tests in thinner Hele-Shaw cells, and by [27, 28, 10] for in which the plates were pulled apart. However, the fingering is stronger and more labyrinthian in structure.

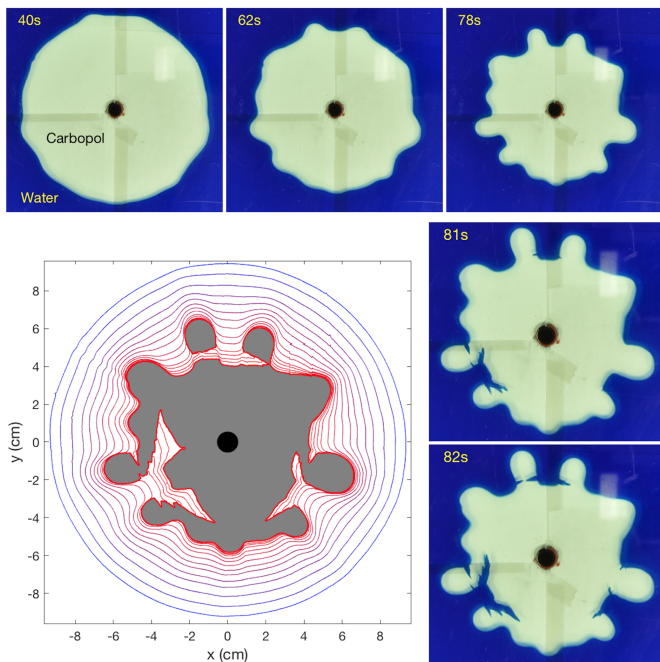


Figure 9: Withdrawal of Carbopol from a cell filled with blue-coloured water. (Pump rate $Q \approx 20\text{ml/min}$; gap $H = 1.7\text{mm}$; rheology $(n, \tau_Y, K) = (0.38, 22\text{Pa}, 13\text{Pa s}^n)$). The images in the top row show the Saffman-Taylor-like pattern which develops relatively slowly; the lower images on the right display rapidly propagating fractures. In the main panel, the interface is plotted at a succession of times, with the colour representing time; the final distribution of Carbopol is shown shaded.

3.2. Fracture patterns

3.2.1. In extraction

When we repeat the extraction experiment (*i.e.* that on the right side of figure 8) with water filling the cell around the Carbopol, the water-Carbopol interface initially evolves much as in the air-displacement test: the interface shrinks around the vent, then suffers a mild fingering instability characterized by angular wavenumbers of $m = 12$ or so; see figure 9. Subsequently, however, a very different behaviour arises in which some of the concave sections of the interface abruptly tear apart, creating to what appear to be fractures of the gel across the entire gap of the Hele-Shaw cell. These fractures then propagate rapidly into the gel at angles close to the azimuthal direction, rather than radially (the direction in which the Saffman-Taylor fingers typically break through to the vent at the end of an air-displacement test). The fractures thereby disfigure the fingering pattern, severing several of the Saffman-Taylor fingers and leaving a rather more complicated looking structure. The locations at which the fractures first form correspond to the positions along the interface with greatest concavity; indeed, the fractures appear to emerge where the interface sharpens almost to a corner, suggestive of the areas with highest tensile stress. Thus, with water as the displacing fluid, the extraction experiment clearly shows a primary, weak Saffman-Taylor-type instability, followed by a secondary, but strong, tearing instability.

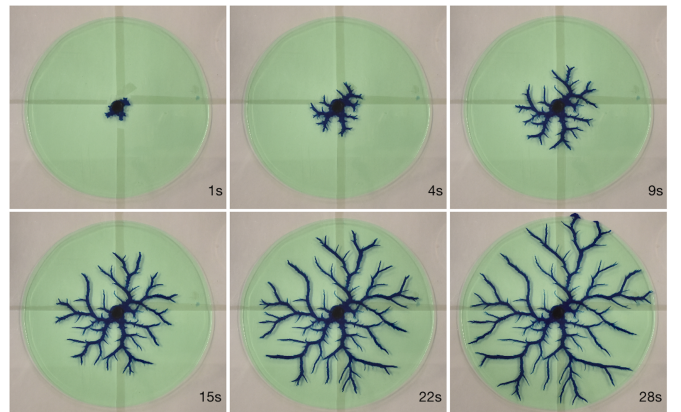


Figure 10: Blue-coloured water pumped into an annulus of (light green) Carbopol in a cell of thickness 3.3mm , with pump rate $Q \approx 40\text{ml/min}$. (Rheology: $n = 0.4$, $\tau_Y = 17\text{Pa}$, $K = 9.8\text{Pa s}^n$).

3.2.2. For a viscoplastic annulus

A similar fracture phenomenon arises when water is pumped into an annulus of Carbopol rather than air. Figures 10-12 display three such tests. The experiment in figure 10 shows the dendritic fracture network that arises from pumping blue-coloured water into a light-green disk of Carbopol. In this example, no weak Saffman-Taylor-like instability appears like that seen on the left of figure 8. Instead, fractures emerge directly from the vent;

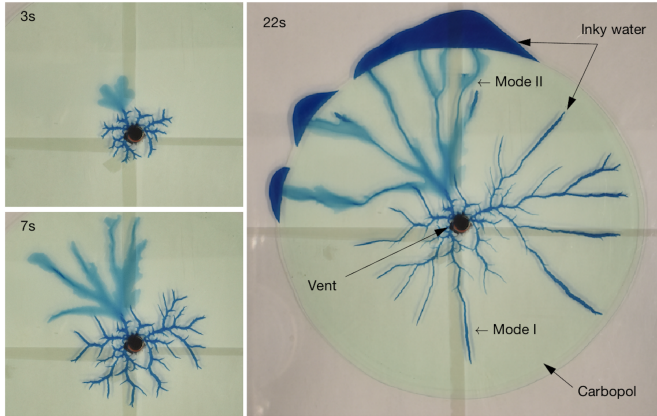


Figure 11: Blue-coloured water pumped into an annulus of (light green) Carbopol in a cell with thickness 1.7mm at pump rate $Q \approx 10\text{ml/min}$. (Rheology: $n = 0.4$, $\tau_Y = 17\text{Pa}$, $K = 9.8\text{Pa s}^n$).

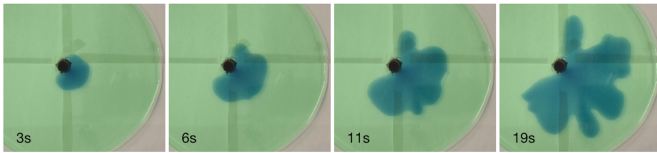


Figure 12: Blue-coloured water pumped into an annulus of (light green) Carbopol in a 4.3mm thick cell at pump rate $Q \approx 10\text{ml/min}$. (Rheology: $n = 0.4$, $\tau_Y = 17\text{Pa}$, $K = 9.8\text{Pa s}^n$).

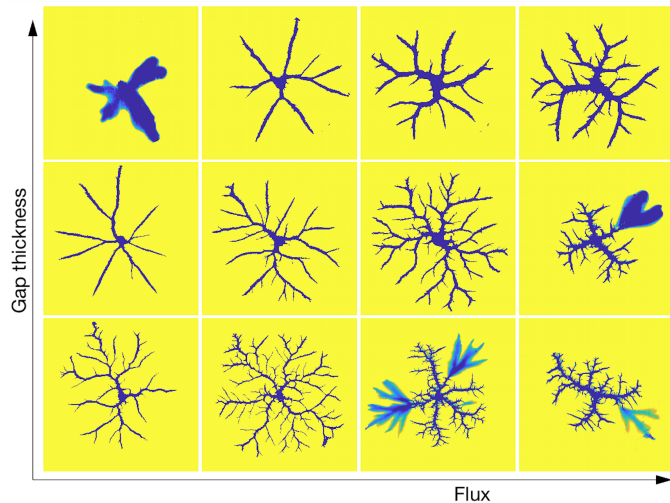


Figure 13: A collage of final fracture patterns for different fluxes (10, 20, 40 and 60 ml/min) and gap thicknesses (1.7, 3.3 and 4.3mm). Pure type-II fracture modes (distinguished by the lighter and broader blue colours) appear in the top left experiment; type-I modes characterize all the others, with the three tests at the bottom right featuring coexisting type-II fractures. (Rheology: $n = 0.4$, $\tau_Y = 17\text{Pa}$, $K = 9.8\text{Pa s}^n$).

the dendritic pattern forms as the fractures, which propagate in almost straight lines, repeatedly split into two conduits of roughly equal size, or spawn multiple smaller side branches without the main conduit changing direction. Overall, the invasive pattern is very different from that in the extraction experiments. The key difference is that

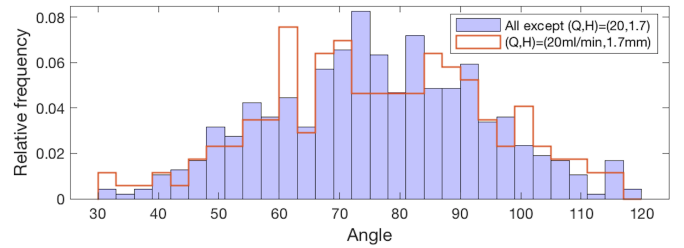


Figure 14: Relative frequency distribution of the angle between split fractures or side branches, showing the experiment with $(Q, H) = (20\text{ml/min}, 1.7\text{mm})$ and the data set taken from all the experiments except that particular test.

the expanding Carbopol annulus is in a state of tension throughout, rather than compression as for the extracted disk. Tearing under tension is therefore immediately possible for the expanding annulus, whereas Saffman-Taylor fingering must develop first for the extracted disk to create locally favourable sites along the interface at which to fracture.

Nevertheless, fractures of this type, in which the gel tears across the whole gap of the Hele-Shaw cell, are not the only possibility. The second experiment, shown in figure 11, displays a second phenomenon: initially a dendritic fracture pattern starts to emerge, but then a more diffuse and wider mode of invasion appears that at first sight is more reminiscent of traditional Saffman-Taylor fingers. The new mode is not, however, a fingering displacement, but is actually a different form of fracturing: the Carbopol now fractures off one of the confining plates, rather than internally across the cell, arising either due to the imposed normal or shear stresses there. In other words, a second, boundary mode of fracturing appears. As evident from the images in the figure, the second mode propagates faster than the first one, with the more diffuse conduits reaching the edge of the Carbopol disk first, thereby draining most of the water pumped into the cell.

Although full-gap fractures characterized many of the displacements in our experiments, the wall mode could also emerge by itself. This is illustrated by the final experiment of figure 12, which also corresponds to the cell with the widest gap. In such cases, it is possible that the gel fractures primarily off the wall below the Carbopol once the water is introduced through the feeder pipe attached to the lower plate, before there is time to tear across the entire gap. Aside from such cases, full-gap fractures form earlier than those along the walls, presumably as a result of higher tensile stress concentrations within the gap. A summary of the final fracture patterns in a suite of experiments in which we varied both the pumping rate and cell thickness is shown in figure 13. Mode-I-type fractures (*i.e.* tears across the slot) feature in all but the thickest cells at the lowest fluxes, which exhibit mode-II-type fractures (against the wall). The two fracture modes co-exist at the highest fluxes in the narrower cells. However, additional experiments, not shown in this figure (but see fig-

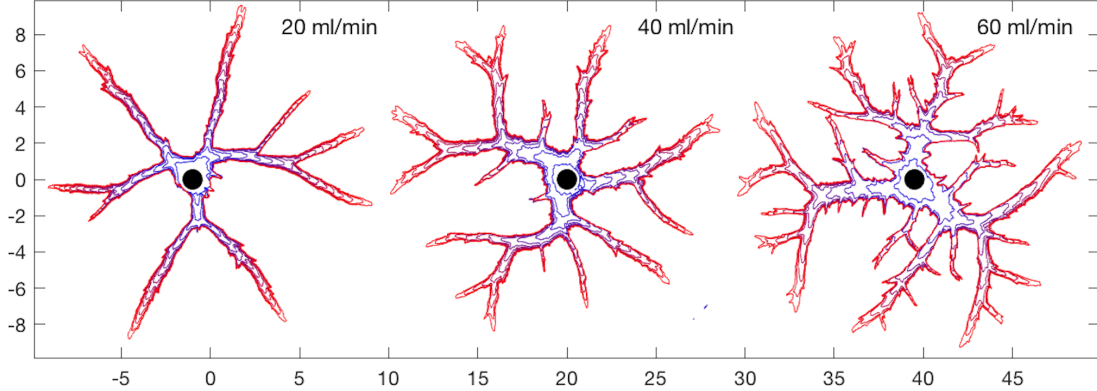


Figure 15: Snapshots of expanding interfaces every 2 seconds in the slot of thickness 4.3mm with the fluxes shown, and colour coded by time. (Rheology: $n = 0.4$, $\tau_Y = 17\text{Pa}$, $K = 9.8\text{Pa s}^n$).

ure 11), also demonstrated that competing fracture modes could arise in the narrower cells at low fluxes, obscuring the conditions favouring each mode. Overall, the number of fractures increases with the flux, due mostly to an enhancement in the frequency at which splittings or side branchings occur, promoting the complexity of the patterns. Another notable feature in figure 13 is that the width of the conduits created by the fractures is relatively insensitive to the flux, but does depend on the gap thickness. All that said, apart from a difference in scale, the patterns are similar along diagonals in the figure.

Measurements of the angles formed when fractures split or side branches appear are shown in figure 14. Each of the tests in figure 13 shows little discernible differences in these angle distributions (the figure compares the measured angles for one of the tests with the corresponding data for all the others), reflecting how the underlying process is insensitive to the flow rate and cell geometry. The distributions show little structure other than a broad peak around 75 degrees and a standard deviation of 20 degrees, over a range from 30 to 120 degrees. This phenomenology is different from that observed in [20] for Hele-Shaw displacement experiments with a colloidal gel, where “visco-elastic” fracture patterns were observed with splitting angles close to 90 degrees.

Additional details of the evolution of the fracture patterns in a subset of the tests (those in the widest cell) are shown in figure 15. Once a fracture appears, the surrounding Carbopol becomes largely arrested, with fluid motion primarily taking place at the fracture tip. The tips of the main fractures advance at roughly constant rate, as seen by the regular spacing of the snapshots of the interface, taken every two seconds. Most of the side branches quickly stop progressing to form dead-ended conduits.

The conduits displayed in figure 15 also maintain a fairly uniform width along their lengths, except at the junctions where the fractures divide. This feature is brought out in more detail in figure 16, which illustrates how conduit widths vary with radial position from the vent for the final patterns of the tests with pure mode-I fractures in figure

13. For simplicity, the widths are extracted by considering the intersections of the fractures with circular arcs (see panel (a)) and so the measured widths are not strictly perpendicular to the conduits. However, the measurements are then averaged over all the fractures to remove any orientation effects, and then plotted against radius (panel (b)). The roughly constant width of the conduit is then evidenced, leading us to take the mean over the radial positions shown in (b). We then plot the result against gap thickness \mathcal{H} in panel (c), bringing out how the conduit width depends on cell geometry (but not flux). In particular, the width appears to be roughly proportional to \mathcal{H} , as in immiscible viscous fingering regularized by surface tension (see §2.2.7 and [2]), or miscible viscous fingering and viscoelastic fracture [3, 18] (although the constant of proportionality looks somewhat different, being closer to 4 there), but unlike linear viscoplastic Saffman-Taylor instability (see §2.2.6 and [7, 8]).

If the fractures open up into conduits of constant width proportional to \mathcal{H} , the constant flux imposed in the experiments demands that the tips must advance linearly in time, as suggested by the uniformly spaced interface snapshots of figure 15. Further evidence for this feature (save for a short transient at early times, and a final phase where the fractures approach the outer edge of the Carbopol) is shown in figure 16(d), which plots the maximum radial extent of the fracture pattern against time. The time required for the pattern to reach a fixed radial position should therefore depend on the combination Q/\mathcal{H}^2 , as seen in panel (e), in which the data for the time to reach a fixed radial position are largely collapsed.

3.2.3. For an interface stable against Saffman-Taylor

Finally, we revisit the problem in which we pump Carbopol into the Hele-Shaw cell, but this time filling the gap with water. The Saffman-Taylor instability is not expected to operate in this setting. However, the interface is in a state of expansion, and therefore tension, which potentially sets the stage for fractures to appear. Indeed, as shown by the example in figure 17, the cracks spanning the

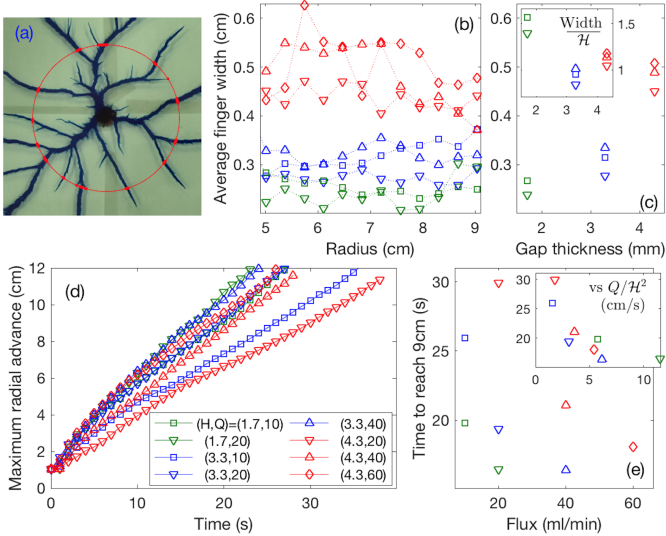


Figure 16: Measurements of conduit width for the final patterns of the tests in figure 13 with pure mode-I fractures. These are extracted by considering the intersection of the fractures with circular arcs (discounting conduits less than about 0.2mm wide; panel (a)). The average width over all the fractures is plotted against radial position from the vent in (b), and then averaged again over radius and plotted against gap thickness in (c). The inset of (c) replots the data, scaling the averaged width by gap thickness \mathcal{H} . In (d), we show the maximum radial advance of the fractures against time for the various tests. The symbol convention used to plot all the data is shown by the legend in this panel. Finally, in (e), we plot the time taken for the fractures to first reach a radius of 9cm against the flux; the inset replots this data against Q/\mathcal{H}^2 .

cell do appear at the interface. These features destroy the axisymmetry of the interface, but remain relatively localized and expand in step with the interface. This results in relatively weak pattern of instability. Note that, in these experiments, to ensure that the interface was circular at the outset of the test, we first pumped a small amount of Carbopol into an empty cell (to a radius of about a centimetre), then poured the water into the rest of the cell around the emplaced disk. We also used suspensions with a wider range of Carbopol concentrations; table 1 lists the parameters of the Herschel-Bulkley fits (we use the yield stress as a convenient label for each).

As illustrated in figures 18 and 19, the degree of non-axisymmetry in the fracture pattern depends on the Carbopol concentration and flux. To quantify this feature, we first observe that the average radius R_{av} of the interface grows with the pumped volume as though it were largely axisymmetric (figure 18(b)). Moreover, the difference between the maximum and minimum radii, R_{max} and R_{min} , scales approximately with R_{av} after an initial transient (figure 18(c-d)). Thus we formulate the average $\langle (R_{max} - R_{min})/R_{av} \rangle$, for volumes over the range, $10 < V < 60$ ml. This diagnostic is plotted against τ_Y and Q in figure 20; additional experiments in cells with different gap width are also shown. Evidently, the implied strength of the pattern decreases with yield stress and flux, and increases with the gap thickness. The scal-

τ_Y (Pa)	51	45	39	35	30	21	8
K (Pa s ⁿ)	29	25	24	23	20	12	6
n	0.38	0.38	0.37	0.36	0.36	0.39	0.41

Table 1: Herschel-Bulkley fits for the different Carbopol concentrations used in the tests of §3.2.3.

ing of R_{max} and R_{min} with R_{av} suggests that the fracture patterns may evolve into a self-similar form; some additional evidence for this is provided in figures 18 and 19, which replots the snapshots of the interface after scaling distance by the maximum radius.

Figure 20 also plots the number of clearly identifiable fractures at the end of the tests, which indicates the typical spacing of these features given that a comparable amount of Carbopol was pumped into the cell each time. The fracture spacing is insensitive to the Carbopol concentration, but certainly decreases as the flux is increased or the gap reduced (*cf.* figures 18 and 19; note that the smaller corrugations evident in the first set of interfaces in figure 19 are not the result of independent fractures, but are the corners of the four primary cracks that become swept sideways by the radial expansion).

A more insidious effect is provided by the plates of the cell themselves: for the most part we used smooth plexiglass for the cell. However, in view of the likely presence of wall slip, we also performed tests with plates that were roughened with sandpaper to reduce any effective sliding. A comparison between tests in smooth and roughened cells is shown in figure 17. The cracks spanning the smooth cell open further in radius and are more numerous around the interface. This suggests that there is an additional containment effect for roughened walls, limiting the development of the fractures, that perhaps results from the elimination of wall slip.

One interesting feature brought out by the plots of the interface at successive instants in figures 18 and 19 is the fractures sometimes isolate almost straight pieces of the interface that become advected out radially without any change of shape. As these sections, and the adjoining, apparently unyielded material, separate from one another under the radial expansion, fresh fluid flows into the gaps, creating distinctive, petal-like structures. The relatively regular spacing of the fracture then lends a flower-like appearance to the fracture pattern.

We close by briefly comparing the Carbopol tests with an experiment with a different viscoplastic fluid: joint compound (a commercially available, kaolin-based material) diluted with water to a concentration where the yield stress is about 50 Pa. Pumping this fluid into an empty Hele-Shaw cell again generates a smooth, axisymmetrically expanding interface. But with water in the cell, the interface rapidly develops a fracture pattern somewhat like in the Carbopol tests; see figure 21. However, for this material the interface appears to have very little integrity, breaking up due to the creation of many fine cracks and developing a rougher appearance. Larger V-shaped cracks

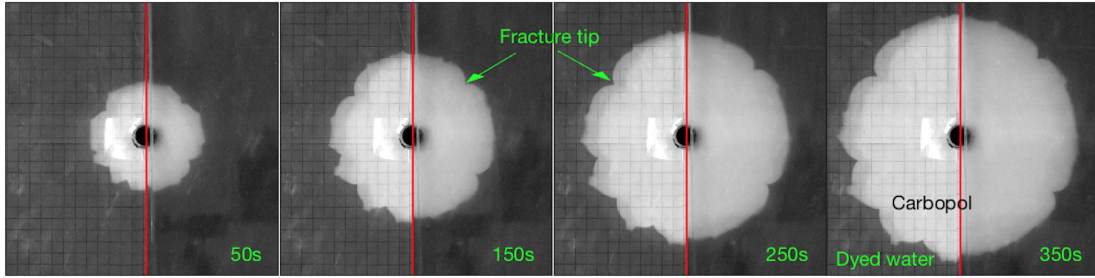


Figure 17: Carbopol (with yield stress 51Pa) pumped into water in a 4.3mm thick cell at pump rate $Q \simeq 20\text{ml/min}$. On the left of each snapshot, the cell has smooth plexiglass walls; on the right, the walls have been roughened with 60-grit sandpaper.

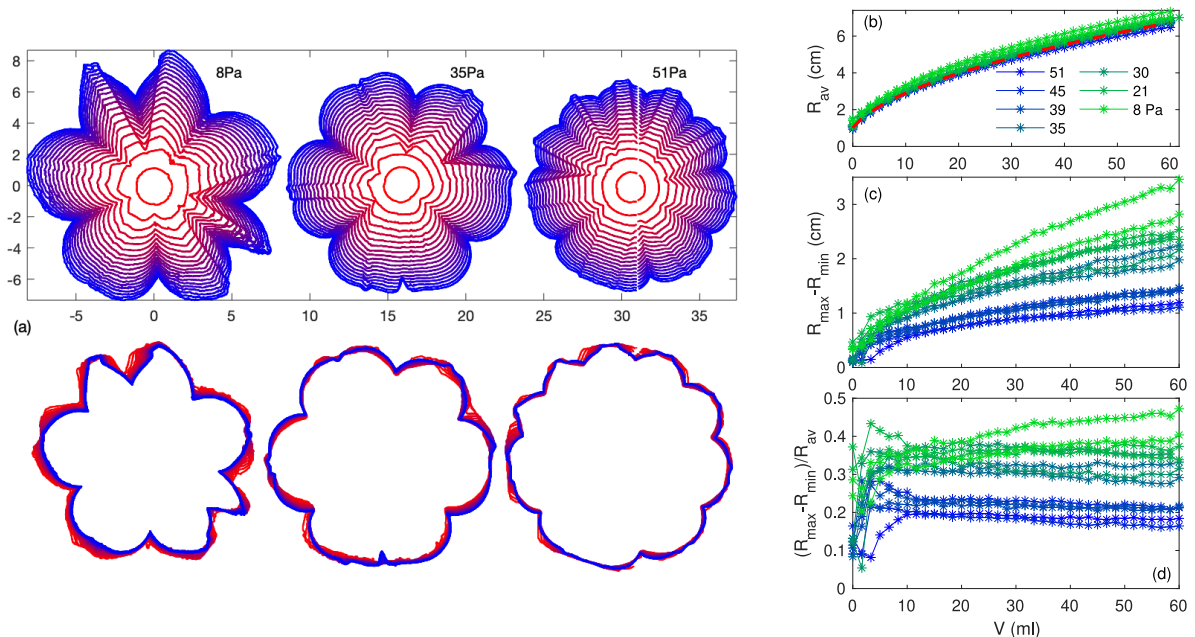


Figure 18: Carbopol with the yield stresses indicated pumped into a 4.3mm thick cell at pump rate $Q \simeq 20\text{ml/min}$. (a) shows snapshots of the interface, equally spaced and coloured by time (with distance measured in cm); the lower plots show the interfaces rescaled by the maximum radius, eliminating the first few to remove the initial transient. On the right, we plot (b) average radius R_{av} , (c) the difference in maximum and minimum radii $R_{max} - R_{min}$ and (d) the scaled different $(R_{max} - R_{min})/R_{av}$, all coloured by τ_Y . The dashed line in (b) shows the expected radius with axisymmetry: $R_{av} = \sqrt{\mathcal{L}^2 + V/(\pi\mathcal{H})}$ if \mathcal{L} is the initial radius.

subsequently develop from some of the fine structure, giving the pattern another flower-like shape. Again, there is evidence for self-similarity: the last images on the right of figure 21 are plotted with an expanding scale (as evidence from the grid on the paper backing to the cell).

Note that the opacity of the joint compound permits us to look for any residual layers of (dyed) water attached to the walls of the cell left behind by the displacing viscoplastic fluid. Such observations do indeed reveal thin layers of water buffering the cell wall near the advancing interface. However, these layers are not wide and appear to end at a water line, implying the joint compound largely displaces the water from the surface. Tests in which Carbopol displaced dark ink showed the same feature. Thus, there appears to be little additional lubrication of the viscoplastic fluids at the plates due to residual wall layers of water.

4. Discussion

In this paper, we have summarized the theoretical analysis of two instabilities that may operate in radial displacements of viscoplastic fluids in Hele-Shaw cells. The first is a recently proposed extensional flow instability that arises in two-dimensional shear-thinning fluids [14, 15]. With the possibility of substantial affective slip, the latter may become relevant in a Hele-Shaw cell. We generalized the linear stability theory for this problem to the Herschel-Bulkley model, thereby incorporating a yield stress and examining the perfectly plastic limit. An important finding of our analysis is that the extensional flow instability is relatively weak, with fairly extreme shear thinning or highly plastic behaviour required to observe its effect in a Hele-Shaw cell, even when the fluid is allowed to slide freely over the walls.

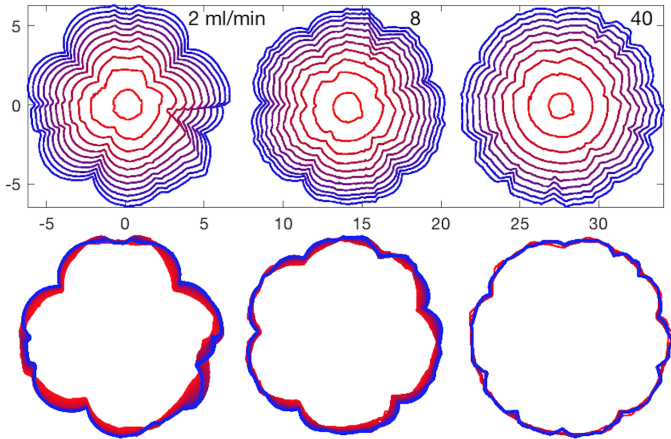


Figure 19: Carbopol with yield stress 51Pa pumped into a 4.3mm thick cell at the fluxes indicated. Shown are snapshots of the interface, equally spaced in the amount of pumped fluid, and coloured by time (with distance measured in cm); the lower plots show the interfaces rescaled by the maximum radius, eliminating the first few to remove the initial transient.

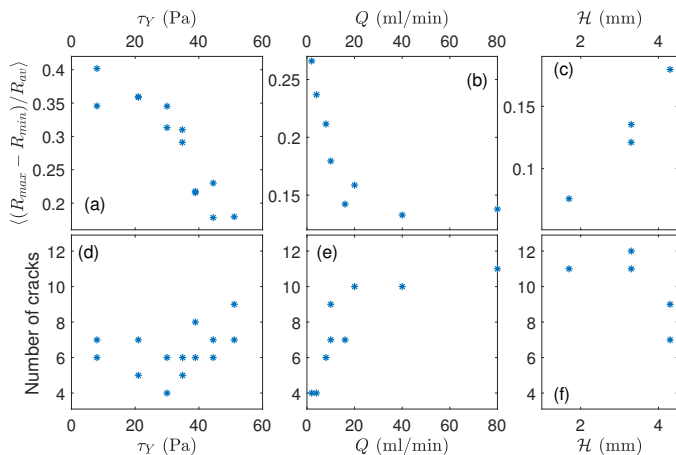


Figure 20: The average scaled radial difference, $\langle (R_{max} - R_{min})/R_{av} \rangle$, for $10 < V < 60$ ml, and number of fractures plotted against (a) τ_Y (for $Q = 10$ ml/min, $\mathcal{H} = 4.3$ mm), (b) Q (for $\tau_Y = 51$ Pa, $\mathcal{H} = 4.3$ mm) and (c) \mathcal{H} (for $Q = 10$ ml/min, $\tau_Y = 51$ Pa).

The second instability is classical Saffman-Taylor fingering, as modified by a yield stress and examined previously by Coussot [7]. In this case, we delved into further details of the stability problem, considering two specific problems involving radial displacements and again studying the perfectly plastic limit.

Our theoretical discussion complements a variety of laboratory experiments conducted with aqueous suspensions of Carbopol displacing or displaced by either air or water. The viscoplastic version of the Saffman-Taylor instability is observed when air is pumped into a cell filled with Carbopol, or when a disk of Carbopol emplaced in the cell is withdrawn. For the former experiments, theoretical predictions appear to be in fair agreement with experimental observations: the most unstable angular wavenumber is roughly consistent with the patterns observed (assuming

interfacial tensions to be comparable to the surface tension of water). Curiously, for the extraction problem, the comparison is less satisfying, with the linear stability theory predicting higher wavenumbers than seen experimentally. Similar discrepancies were observed by Derks *et al.* [28] in plate-separation experiments.

Both experiments show dramatic differences when performed with water as the second fluid: in the extraction experiment, a similar viscoplastic Saffman-Taylor instability is observed initially. Although the angular wavenumbers are slightly higher than for air displacement, they are not significantly so, which is surprising in view of the fact that the two fluids are now miscible. Interfacial tension effects are therefore minimal, and so the most unstable wavelengths are expected to scale down to the thickness of the cell [3]. This surprise is compounded by a secondary instability that appears when the finger pattern has developed sufficiently to create concave sections of the interface. The tension generated over these pieces of the interface then causes the Carbopol to fracture; the cracks rapidly propagate in an almost angular direction, severing fingers and disfiguring the pattern.

In the experiments in which water is pumped into a Carbopol-filled cell, the entire expanding interface is under tension and the fractures form immediately, supplanting any Saffman-Taylor fingering. Dendritic fracture patterns then advance rapidly into the cell. Two types of fractures are observed: the most common consist of cracks across the cell, but a second variety can also appear in which the Carbopol fractures off the cell walls.

The fractures do not occur when other immiscible fluids are used instead of water, with Saffman-Taylor fingers appearing much like in the air displacement experiments. Also, the fractures are not sensitive to whether the water was distilled, taken directly from a tap, or coloured with ink. We further added sugar to raise the viscosity by up to a factor of about ten (and potentially change the interfacial interaction with the Carbopol), with no qualitative effect on the fracturing and a minimal quantitative one. The experiments therefore clearly distinguish Saffman-Taylor fingering from fracture patterns, and suggest the main property of the second fluid that is required for the latter is that it is water-based.

When Carbopol was pumped into an air-filled cell, the interface remained axisymmetrical, as expected from the absence of the Saffman-Taylor instability in this configuration and our theoretical prediction that the shear-thinning extensional flow instability was insignificant even under extreme wall slip. Once more, however, pumping Carbopol into a water-filled can lead to non-axisymmetrical patterns. The culprit was again the fracturing of the expanding interface under tension. In this setting the fractures do not develop strongly but remain localized close to the interface, becoming effectively contained by the yield stress of the fluid, the narrow gap and the inability to slide freely over the cell walls.

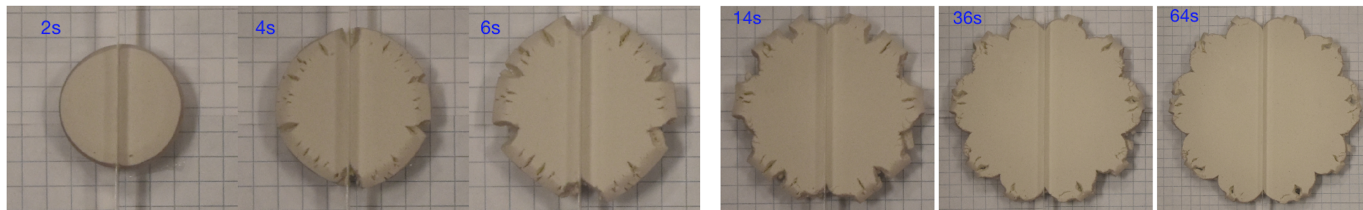


Figure 21: Joint compound with a yield stress of around 50 Pa. On the left, the images have the same scale; on the right, the images are cropped to bring out the structure of the edge and self-similar evolution (the scale can be judged from the size of the grid on the paper backing to the cell).

Acknowledgements We thank Mark Martinez, Stephen Morris, Roiy Sayag and Grae Worster for useful discussions.

Declaration of Competing Interest We declare no conflict of interests.

References:

- [1] P. G. Saffman, G. I. Taylor, The penetration of a fluid into a porous medium or Hele-Shaw cell containing a more viscous liquid, *Proceedings of the Royal Society of London. Series A. Mathematical and Physical Sciences* 245 (1242) (1958) 312–329.
- [2] L. Paterson, Radial fingering in a Hele-Shaw cell, *Journal of Fluid Mechanics* 113 (1981) 513–529.
- [3] L. Paterson, Fingering with miscible fluids in a Hele-Shaw cell, *The Physics of fluids* 28 (1) (1985) 26–30.
- [4] S. D. R. Wilson, A note on the measurement of dynamic contact angles, *Journal of Colloid and Interface Science* 51 (3) (1975) 532–534.
- [5] S. D. R. Wilson, The Taylor–Saffman problem for a non-Newtonian liquid, *Journal of Fluid Mechanics* 220 (1990) 413–425.
- [6] L. Kondic, M. J. Shelley, P. Palffy-Muhoray, Non-Newtonian Hele-Shaw flow and the Saffman–Taylor instability, *Physical Review Letters* 80 (7) (1998) 1433.
- [7] P. Coussot, Saffman–Taylor instability in yield-stress fluids, *Journal of Fluid Mechanics* 380 (1999) 363–376.
- [8] A. Lindner, P. Coussot, D. Bonn, Viscous fingering in a yield stress fluid, *Physical Review Letters* 85 (2) (2000) 314.
- [9] N. Maleki-Jirsaraei, A. Lindner, S. Rouhani, D. Bonn, Saffman–Taylor instability in yield stress fluids, *Journal of Physics: Condensed Matter* 17 (14) (2005) S1219.
- [10] O. A. Fadoul, P. Coussot, Saffman–Taylor instability in yield stress fluids: Theory–experiment comparison, *Fluids* 4 (1) (2019) 53.
- [11] J. V. Fontana, S. A. Lira, J. A. Miranda, Radial viscous fingering in yield stress fluids: Onset of pattern formation, *Physical Review E* 87 (1) (2013) 013016.
- [12] A. Eslami, S. M. Taghavi, Viscous fingering of yield stress fluids: The effects of wettability, *Journal of Non-Newtonian Fluid Mechanics* 264 (2019) 25–47.
- [13] B. Ebrahimi, P. Mostaghimi, H. Gholamian, K. Sadeghy, Viscous fingering in yield stress fluids: a numerical study, *Journal of Engineering Mathematics* 97 (1) (2016) 161–176.
- [14] R. Sayag, M. G. Worster, Instability of radially spreading extensional flows. Part 1: Experimental analysis, *Journal of Fluid Mechanics* 881 (2019) 722–738.
- [15] R. Sayag, M. G. Worster, Instability of radially spreading extensional flows. Part 2: Theoretical analysis, *Journal of Fluid Mechanics* 881 (2019) 739–771.
- [16] H. A. Barnes, A review of the slip (wall depletion) of polymer solutions, emulsions and particle suspensions in viscometers: its cause, character, and cure, *Journal of Non-Newtonian Fluid Mechanics* 56 (3) (1995) 221–251.
- [17] Y. Liu, N. J. Balmforth, S. Hormozi, Axisymmetric viscoplastic dambreaks and the slump test, *Journal of Non-Newtonian Fluid Mechanics* 258 (2018) 45–57.
- [18] H. Van Damme, C. Laroche, L. Gatinéau, P. Levitz, Viscoelastic effects in fingering between miscible fluids, *Journal de Physique* 48 (7) (1987) 1121–1133.
- [19] H. Van Damme, C. Laroche, L. Gatinéau, Radial fingering in viscoelastic media, an experimental study, *Revue de physique appliquée* 22 (4) (1987) 241–252.
- [20] E. Lemaire, P. Levitz, G. Daccord, H. Van Damme, From viscous fingering to viscoelastic fracturing in colloidal fluids, *Physical review letters* 67 (15) (1991) 2009.
- [21] H. Zhao, J. V. Maher, Associating-polymer effects in a Hele-Shaw experiment, *Physical Review E* 47 (6) (1993) 4278.
- [22] T. Baumberger, C. Caroli, D. Martina, Solvent control of crack dynamics in a reversible hydrogel, *Nature materials* 5 (7) (2006) 552–555.
- [23] T. Baumberger, C. Caroli, D. Martina, Fracture of a biopolymer gel as a viscoplastic disentanglement process, *The European Physical Journal E* 21 (1) (2006) 81–89.
- [24] T. Baumberger, O. Ronsin, A convective instability mechanism for quasistatic crack branching in a hydrogel, *The European Physical Journal E* 31 (1) (2010) 51–58.
- [25] D. R. Hewitt, M. Daneshi, N. J. Balmforth, D. M. Martinez, Obstructed and channelized viscoplastic flow in a Hele-Shaw cell, *Journal of Fluid Mechanics* 790 (2016) 173–204.
- [26] S. S. Cardoso, A. W. Woods, The formation of drops through viscous instability, *Journal of Fluid Mechanics* 289 (1995) 351–378.
- [27] Q. Barral, G. Ovarlez, X. Chateau, J. Boujlel, B. Rabideau, P. Coussot, Adhesion of yield stress fluids, *Soft Matter* 6 (6) (2010) 1343–1351.
- [28] D. Derks, A. Lindner, C. Creton, D. Bonn, Cohesive failure of thin layers of soft model adhesives under tension, *Journal of applied physics* 93 (3) (2003) 1557–1566.